Mars InSight Entry, Descent, and Landing Trajectory and Atmosphere Reconstruction

Christopher D. Karlgaard*
Analytical Mechanics Associates, Inc., Hampton, VA, 23666

Ashley M. Korzun† and Mark Schoenenberger‡
NASA Langley Research Center, Hampton, VA, 23681

Eugene P. Bonfiglio§, David M. Kass¶ and Myron R. Grover‖
Jet Propulsion Laboratory, California Institute of Technology, Pasadena, CA, 91109

The InSight mission landed on the surface of Mars on November 26th, 2018. The InSight system performance met all design requirements, although several performance metrics fell near the boundaries of the predictions. The peak deceleration was high, the overall timeline was short, and the landing site was uprange and crossrange from the target. This paper describes the reconstruction of the entry, descent, and landing trajectory and atmosphere. The approach utilizes a Kalman filter to blend sensor data to obtain the vehicle trajectory. The aerodynamic database is used in combination with the sensed accelerations to obtain estimates of the atmosphere-relative state, which in turn is used to derive the free-stream atmospheric conditions during entry, until the time of parachute deployment. The results indicate that the reconstructed atmosphere was approximately 1σ below the preflight atmosphere. Analysis of the reconstructed vehicle attitude angles indicate that the aerodynamic lift was oriented downward at entry. The vehicle developed a roll rate during entry, which directed a component of the lift to the north. The low density and aerodynamic lift direction are determined to be the primary causes of the high deceleration, short timeline, and location of the landing site relative to the target.

Nomenclature

C_A, C_Y, C_N	=	Axial, side, and normal aerodynamic force coefficients
$\boldsymbol{P}_0$	=	EMEJ2000 position and velocity covariance at t_0
$\Re$	=	Specific gas constant, J/kg-K
$\boldsymbol{r}_{imu}$	=	Position of the IMU in the cruise frame, m
T_{cr2b}	=	Cruise frame to body frame transformation matrix
T_{imu2cr}	=	IMU instrument frame to cruise frame transformation matrix
t	=	Time, s
t_0	=	Initial time, s
X, Y, Z	=	EMEJ2000 position components at t_0
$\dot{X}$, $\dot{Y}$, $\dot{Z}$	=	EMEJ2000 velocity components at t_0
α	=	Angle of attack, rad
α_T	=	Total angle of attack, rad
β	=	Angle of sideslip, rad
ζ_0, ζ_1, ζ_2, ζ_3	=	Quaternion components of the EMEJ2000 to cruise frame attitude at t_0
ν_0, ν_1, ν_2, ν_3	=	Quaternion components of the EMEJ2000 to MCMF attitude at t_0

*Supervising Engineer, Associate Fellow AIAA.
†Research Aerospace Engineer, Atmospheric Flight and Entry Systems Branch, Member AIAA.
‡Aerospace Engineer, Atmospheric Flight and Entry Systems Branch, Senior Member AIAA.
§Senior Engineer, Guidance, Navigation, and Control Section.
¶Planetary Scientist, Planetary and Exoplanetary Atmospheres.
‖Senior Aerospace Engineer, EDL Systems Advanced Technologies Group, Member AIAA.

I. Introduction

THE InSight mission landed on the surface of Mars on November 26th, 2018. The spacecraft is a stationary lander with an suite of instruments designed to study the interior of Mars [1]. The InSight mission made use of an architecture similar to that of the Phoenix mission, which placed a stationary lander on the surface of Mars on May 28th, 2008 [2]. The Mars InSight entry vehicle is a 70 deg sphere-cone shape with a diameter of 2.65 m and mass at entry of 605.6 kg. The Entry, Descent, and Landing (EDL) concept of operations is shown in Figure 1. The nominal velocity and flight path angle at entry are 5.5 km/s and -12.0 deg. During the hypersonic phase the ballistic entry vehicle is unguided and is not spin stabilized. After passing peak heating and peak deceleration the vehicle slows to a Mach number of approximately 1.56 where the supersonic disk-gap-band parachute is deployed. Shortly thereafter the heatshield is jettisoned, lander legs are deployed, the radar altimeter is activated, and the lander separates from the backshell and begins powered flight. During the terminal descent phase the lander flies on a gravity turn trajectory until reaching a condition close to the landing site, where it descends at a constant velocity until touchdown after which the motor is powered off.

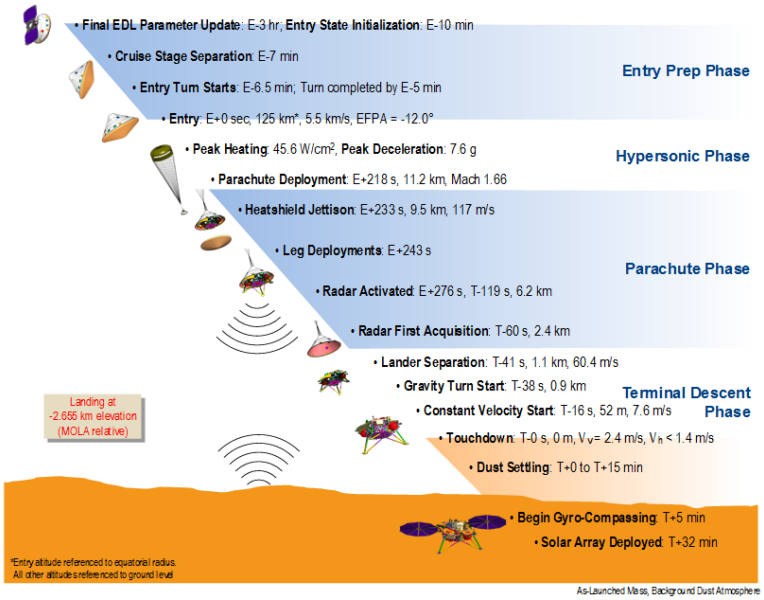

Fig. 1 InSight Entry, Descent, and Landing Concept of Operations

The InSight EDL system performance met all design requirements although several performance metrics fell on either the low or high end of the pre-flight predictions, based on 6-DOF flight mechanics simulations [3]. In particular the observed peak deceleration was 8.25 g's whereas the 99% prediction was 8.1 g's. The system requirement was to be below 13 g's. The overall duration of the EDL timeline was short at 349.0 s whereas the 1% prediction was 341.5 s. The vehicle landed at a point 12.3 km uprange and 6.1 km crossrange of the target site, relative to a 77.4 km by 23.1 km landing ellipse prediction based on the last orbit determination solution.

This paper describes the reconstruction of the InSight EDL as-flown trajectory and atmosphere. The approach is similar to that used for reconstructing the Phoenix EDL performance [4] in which a Kalman filter [5] reconstruction method is used to blend on-board sensor data sources to produce an estimate of the vehicle trajectory through inertial space. These data sources include on-board accelerations and angular rates from the inertial measurement unit (IMU) at a rate of 200 Hz and radar altimeter measurements recorded after heatshield jettison from an altitude of approximately 2.4 km to the surface at a rate of 10 Hz. These measurements are combined with initial conditions based on orbit determination solutions and the post-landing position fix to provide the initial and final positions of the trajectory. The next step of the process makes use of the reconstructed trajectory, sensed acceleration measurements, and the nominal aerodynamic database to reconstruct the atmospheric conditions.

The remainder of this paper is organized as follows. Section II describes several coordinate frames that are used for the reconstruction of the InSight EDL trajectory. Section III discusses the data sources that are used for the reconstruction, and Section IV describes the methodology used to perform the reconstruction. The results of the reconstruction are described in Section V.

II. Coordinate Frames

The Earth Mean Equator and Equinox of Epoch January 2000 (EMEJ2000) [6] inertial reference system is defined by the Z axis normal to the Earth mean equator at the epoch of J2000 (Julian date of 2451545.0) and the X axis parallel to the vernal equinox of the Earth mean orbit at J2000. The Mars-Centered Mars-Fixed (MCMF) frame is defined by the Z axis normal to the equator of Mars and the X axis aligned through the prime meridian. In each frame, the Y axis is chosen to complete the right-handed system.

The Areocentric (AC) frame has its origin at the vehicle center of mass, with the Z axis oriented toward the center of the planet, the X axis normal to the radius vector in the northerly direction, and Y axis is to the East. The Areodetic (AD) frame is defined similarly to the AC frame but has its Z axis perpendicular to the reference ellipse and X axis tangent to the reference ellipse in the north direction. The Y axis of the AD frame is the same as that of the AC frame. The Areodetic frame is also commonly referred to as the North-East-Down (NED) frame.

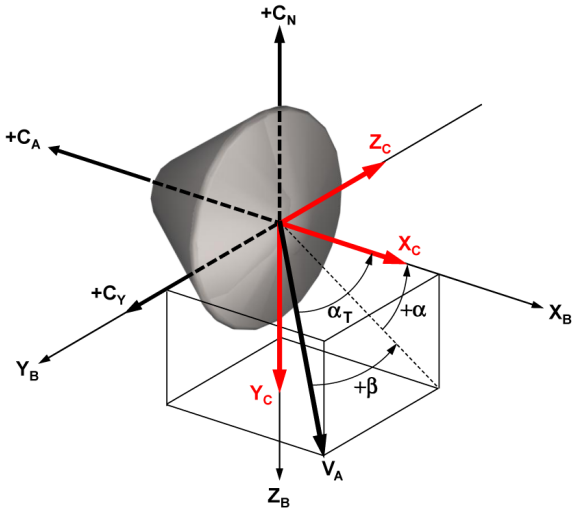

Fig. 2 InSight Vehicle Coordinate Frames

Vehicle coordinate frames relevant to the aerodynamics and flight mechanics are shown in Figure 2. The axes labeled X_C, Y_C, and Z_C are the axes of the cruise frame and the axes labeled X_B, Y_B, and Z_B define the flight mechanics body frame. Directions of the aerodynamic force coefficients C_A, C_Y, and C_N are shown relative to the flight mechanics body frame as are the definitions of the aerodynamic flow angles. The transformation from cruise frame to the flight mechanics body frame is given by

$$T_{cr2b} = \begin{bmatrix} 1 & 0 & 0 \\ 0 & 0 & -1 \\ 0 & 1 & 0 \end{bmatrix} \tag{1}$$

The IMU instrument frame is defined by the axes internal to the IMU in which the three-axis accelerations and angular rates are measured. The location of the IMU in the cruise reference frame is given by the vector $\boldsymbol{r}_{imu} = [\ 0.9952 \quad 0.6470 \quad -0.3955\ ]^T$ m. The transformation from the IMU instrument frame to the cruise reference frame is given by the matrix

$$T_{imu2cr} = \begin{bmatrix} -0.999998485671136 & 0.0001357467181835186 & 0.001735000918828398 \\ 0.0007450526093386297 & 0.9343638812743024 & 0.3563194946485962 \\ -0.001572752990507626 & 0.3563202477306758 & -0.934362567478589 \end{bmatrix} \tag{2}$$

III. Data Sources

A. Inertial Measurement Unit

The primary measurement source for performing the trajectory and atmosphere reconstruction is the on-board IMU, a Honeywell Miniature Inertial Measurement Unit (MIMU), consisting of QA3000 accelerometers and GG1320

ring laser gyroscopes. The MIMU provides three-axis linear acceleration and angular rate measurements in the IMU instrument frame at a sample rate of 200 Hz. The measured accelerations were transformed from the IMU frame into the vehicle body frame using the transformation matrices given in 1 and 2 for integration in order to propagate the states from the initial condition. The integration scheme accounts for the IMU position offset and transforms the accelerations to the vehicle center of mass.

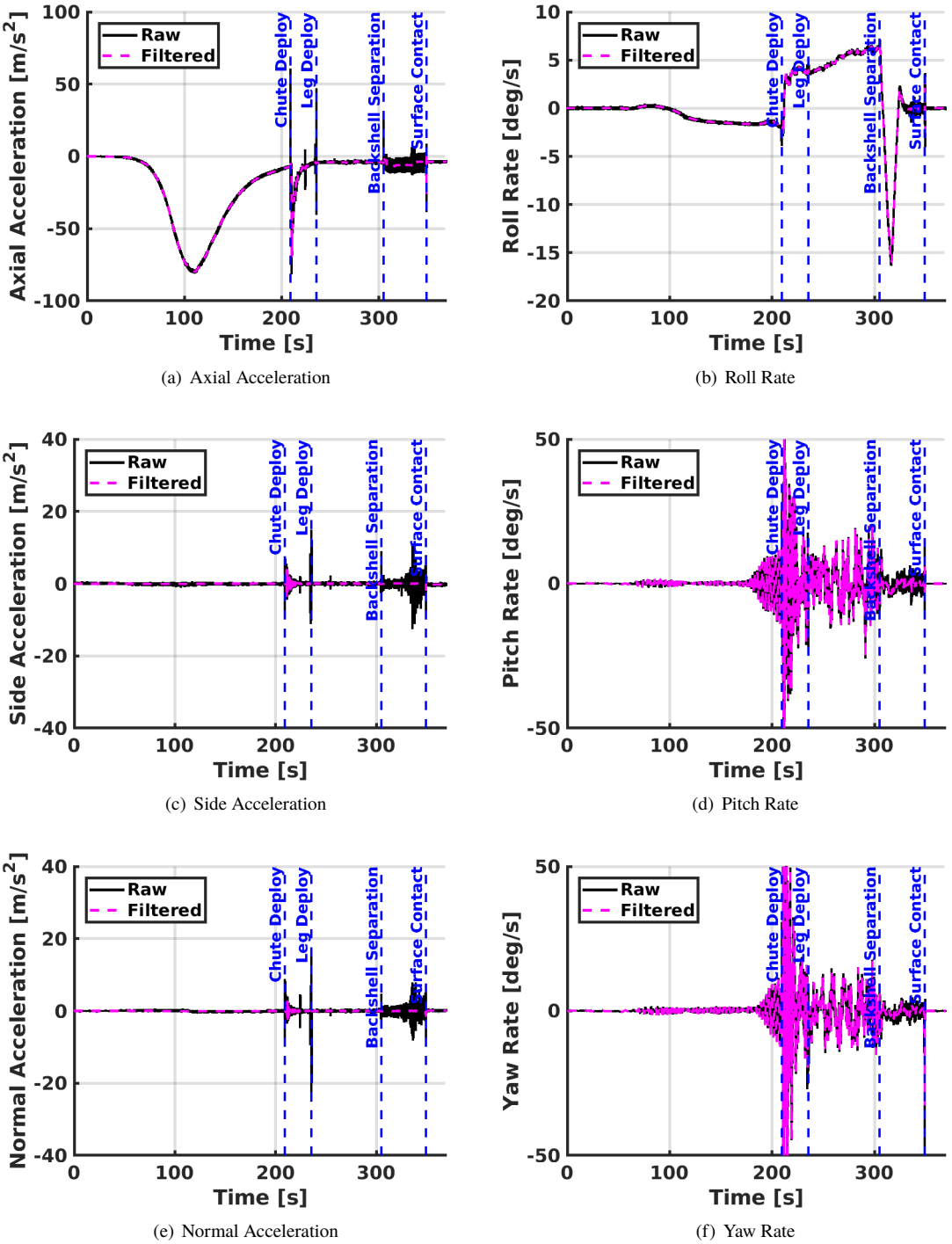

(a) Axial Acceleration

(b) Roll Rate

(c) Side Acceleration

(d) Pitch Rate

(e) Normal Acceleration

(f) Yaw Rate

Fig. 3 Accelerations and Angular Rates in Flight Mechanics Body Frame

Note that the numerical integration of these data for propagating the vehicle state makes use of the raw accelerations with no filtering. A second-order Butterworth filter [7] with a 5 Hz cutoff frequency is also applied to smooth the data for use in the atmospheric reconstruction. The filter is applied in forward/backward mode to eliminate phase loss. The raw and filtered accelerations and angular rates are shown in Figure 3.

The MIMU was modeled using the error parameters specified in Table 1 provided in [8] and the quantization specifications in [9]. These uncertainties were modeled as consider parameters in the Kalman filter so that the reconstructed state uncertainties are more realistic based on the accelerometer and gyroscope measurement uncertainties.

Table 1 IMU Error Parameters

Error Parameter	Accelerometer	Gyroscope
Misalignment (3σ)	0.05 deg	0.05 deg
Noise (3σ)	150 μg	0.0042 deg/s
Scale Factor (3σ)	525 ppm	15 ppm
Bias (3σ)	300 μg	0.15 deg/hour
Quantization	0.54 m/s^2	0.0115 deg/s

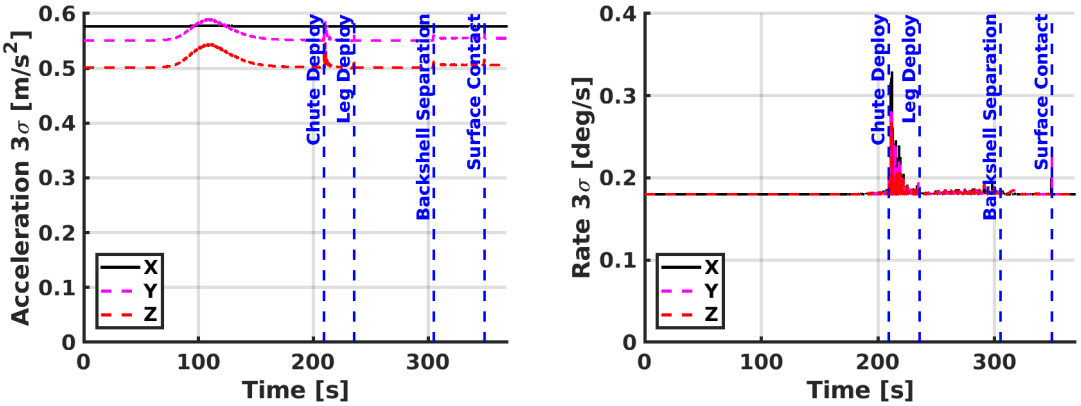

(a) Acceleration (b) Angular Rate

Fig. 4 Acceleration and Angular Rate Uncertainties

B. Radar Altimeter

After heatshield separation, the on-board radar altimeter (a modified Honeywell HG9580 [10]) was activated to measure the above ground level altitude of the vehicle during the terminal descent phase. These measurements were used in the trajectory reconstruction process to provide position data that can be processed by the Kalman filter to improve the trajectory estimate. The radar altimeter measurements are shown in Figure 5. The measurements are assumed to be accurate to within 5% (3σ) with a resolution of 0.31 m [10].

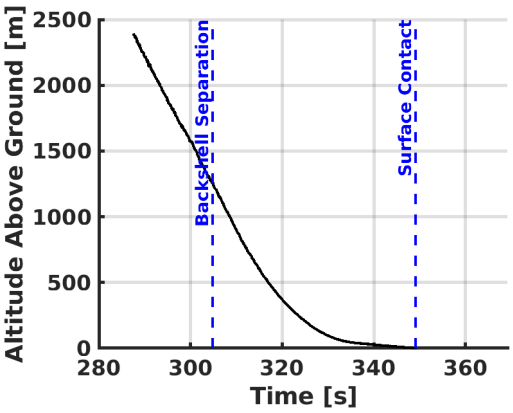

Fig. 5 Radar Altimeter Data

C. Initial Conditions

The initial conditions used for the reconstruction are based on the orbit determination (OD) solution OD133 [11, 12], which were adjusted to compensate for the small impulse imparted to the entry vehicle at cruise stage separation prior to entry. The states are provided in the EMEJ2000 inertial frame at a spacecraft clock time (SCLK) of t_0 = 596533118.7115 s. These coordinates correspond to a radius from the center of the planet of 3522.14 km. The position and velocity components are listed in Table 2. The covariance of the EMEJ2000 initial states is given in Equation 3.

Table 2 EMEJ2000 Orbit Determination 133 Initial Conditions

Coordinate	Initial Condition
X, m	-3482035.47264304
Y, m	520044.864332262
Z, m	102229.701715811
$\dot{X}$, m/s	416.584594960206
$\dot{Y}$, m/s	-5603.34249567148
$\dot{Z}$, m/s	1270.31257657616

$$\boldsymbol{P}_0 = \begin{bmatrix} 6.7958 & -1.1424\text{e}{-1} & -3.6705\text{e}1 & -2.9613\text{e}{-3} & 4.2592\text{e}{-3} & 1.4140\text{e}{-2} \\ -1.1424\text{e}{-1} & 7.5547 & 1.1729\text{e}2 & 1.4171\text{e}{-3} & -9.1147\text{e}{-3} & -2.2991\text{e}{-2} \\ -3.6705\text{e}1 & 1.1729\text{e}2 & 2.5588\text{e}3 & 7.6232\text{e}{-2} & -2.4089\text{e}{-1} & -6.2291\text{e}{-1} \\ -2.9613\text{e}{-3} & 1.4171\text{e}{-3} & 7.6232\text{e}{-2} & 4.4306\text{e}{-6} & -9.0562\text{e}{-6} & -2.4297\text{e}{-5} \\ 4.2592\text{e}{-3} & -9.1147\text{e}{-3} & -2.4089\text{e}{-1} & -9.0562\text{e}{-6} & 2.4504\text{e}{-5} & 6.3641\text{e}{-5} \\ 1.4140\text{e}{-2} & -2.2991\text{e}{-2} & -6.2291\text{e}{-1} & -2.4297\text{e}{-5} & 6.3641\text{e}{-5} & 1.6698\text{e}{-4} \end{bmatrix} \tag{3}$$

The attitude initial conditions were extracted from the onboard navigation state contained within the InSight telemetry data. The attitude is based on a star tracker initialization prior to cruise stage separation that is then propagated forward in time based on the IMU gyroscope measurements. The attitude conditions at t_0 are listed in Table 3. The 3σ uncertainties are assumed to be 0.25 deg in each axis, uncorrelated.

The orientation of Mars with respect to the EMEJ2000 frame is also required in order to compute the planet-relative trajectory. The MCMF frame is defined relative to the EMEJ2000 frame at t_0 by the quaternion listed in Table 4.

Table 3 EMEJ2000 Cruise Frame Attitude Initial Conditions

Quaternion	Initial Condition
ζ_0	0.103127965380345
ζ_1	0.721053695075494
ζ_2	-0.683489133451464
ζ_3	0.0478413631521303

Table 4 EMEJ2000 MCMF Frame Initial Conditions

Quaternion	Initial Condition
ν_0	0.917055674387943
ν_1	$-4.689\,339\,376\,369\,31\text{e}{-5}$
ν_2	0.000133110931331978
ν_3	-0.398759163098936

D. Landing Site Location

The InSight landing site location is shown in Table 5. This landing site corresponds to a Mars Orbiter Laser Altimeter (MOLA) [13] elevation of -2613.43 m. This location is used for trajectory reconstruction purposes to provide an end point to the trajectory as another form of a position fix. The landing site was determined by matching features from lander images with those captured from High Resolution Imaging Science Experiment (HiRISE) [14] onboard the Mars Reconnaissance Orbiter (MRO).

Table 5 InSight Landing Site Coordinates

Coordinate	Value	3σ
Radius	3393079.5 m	5 m
Longitude	135.62343 deg	0.000337 deg
Declination	4.50238 deg	0.000471 deg

E. Mass Properties Model

The vehicle mass properties were reconstructed based on the as-flown timeline and commanded thruster firing history. The vehicle mass, inertia, fuel mass for each tank, and vehicle center of mass location were constructed as a function of the vehicle timeline at a sample rate of 10 Hz. The reconstructed total vehicle mass is shown in Figure 6.

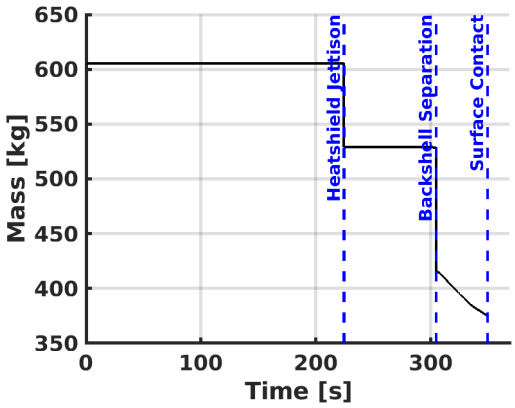

Fig. 6 Vehicle Mass

F. Atmosphere Model

An atmospheric model is available based on data taken from the Mars Climate Sounder (MCS) instrument [15] onboard the MRO. The profile, labeled MCS 4.24, was obtained two days prior to landing at a spatial location above the landing site. The profile provides density, pressure, and temperature as a function of MOLA altitude. An atmosphere model [16] was used to generate dispersed profiles centered around the nominal MCS 4.24 profile. An ensemble of 100,000 dispersed cases were generated about the nominal MCS 4.24 profile. The mean profile and the 3σ bounds of the ensemble distributions are shown in Figure 7.

The atmospheric winds assumed for the trajectory reconstruction are based on a preflight wind model. The wind model included 8000 dispersed profiles that were used for preflight trajectory Monte Carlo analysis. The mean wind profile and the 3σ bounds of the distributions are shown in Figure 7. Note that the wind dispersions are uncorrelated to the atmospheric dispersions in the model.

Instrumentation in the InSight Auxiliary Payload Sensor Suite (APSS) [17] include atmospheric pressure sensors to be used for atmospheric science [18]. Surface pressure data at the landing local mean solar time were gathered for Sols 14 through 40 after landing. A linear fit was performed on this data, which was then extrapolated back to the landing time on Sol 0. The result is a surface pressure of 733.724 Pa with a 3σ uncertainty of 6.865 Pa. The extrapolation is in agreement with measurements from the Mars Science Laboratory (MSL) Rover Environmental Monitoring Station (REMS) [19] that were scaled for the altitude difference, resulting in a pressure of 733.131 Pa. The surface pressure measurement data are shown in Figure 8.

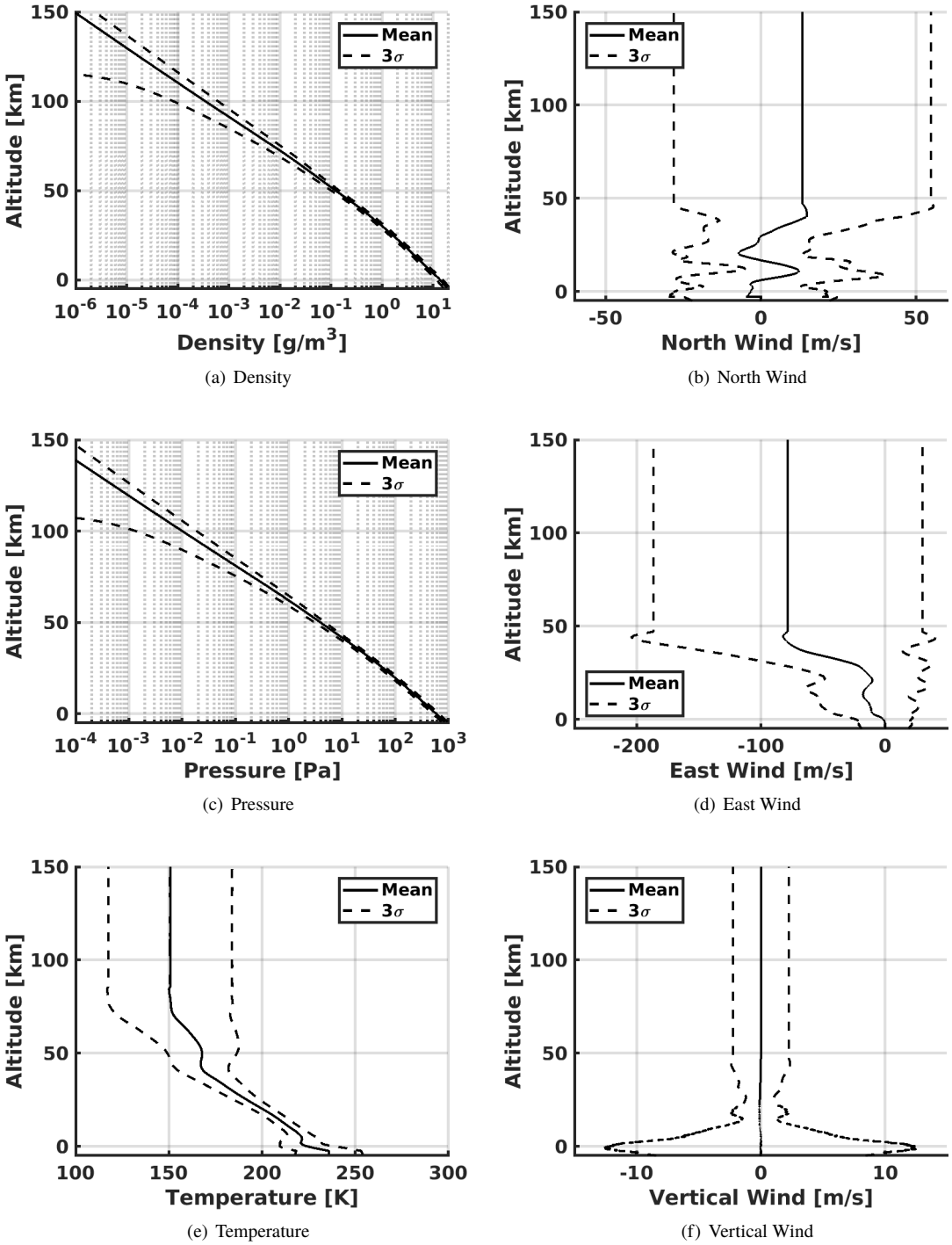

(a) Density

(b) North Wind

(c) Pressure

(d) East Wind

(e) Temperature

(f) Vertical Wind

Fig. 7 Atmosphere and Winds

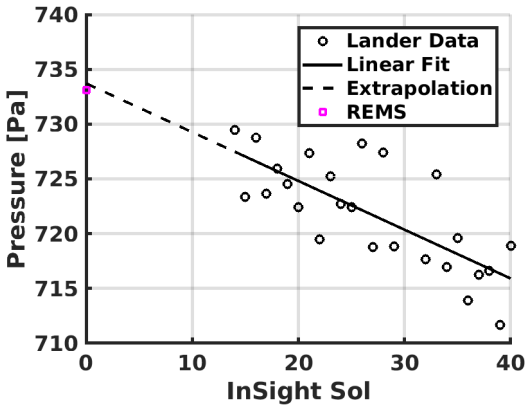

Fig. 8 InSight Surface Pressure

G. Aerodynamics Model

The aerodynamics database for InSight is identical to that developed for Phoenix. The aerodynamics database was built using computational methods and best practices originally established for Mars Pathfinder and data from the Mars Exploration Rover (MER) and Viking programs. Aerodynamics coefficients were provided as functions of total angle of attack and Knudsen number, velocity, or Mach number, depending on the flight regime [20]. High-altitude (non-continuum) coefficients, as well as dynamic damping characteristics, were taken from MER testing and analysis. Hypersonic static coefficients were generated with non-equilibrium Navier-Stokes computational fluid dynamics (CFD). Supersonic static coefficients were developed using CFD on the forebody and a Viking-derived pressure correction for aftbody contributions [20]. Uncertainties were unchanged from Phoenix, deriving heritage from Mars Pathfinder and MER [21, 22].

H. Gravity Model

The Mars gravitational acceleration is modeled using the MRO110C model [23]. This model is based on tracking data of Mars Global Surveyor (MGS), Mars Odyssey, MRO, and MOLA-derived topography data. The model contains spherical harmonics up to degree and order 110.

IV. Reconstruction Methods

A. Trajectory Reconstruction

The InSight EDL trajectory was reconstructed using an Iterative Extended Kalman Filter (IEKF) code that computes six degree of freedom trajectory estimates based on the available measurement data and associated uncertainties. The filter is formulated as a fixed-interval smoother that merges a forward and backward pass through the data so that each data point in the trajectory is estimated from the entire set of available data. The approach uses a modernized implementation of the Statistical Trajectory Estimation Program (STEP) [24, 25] known as NewSTEP [26–30]. NewSTEP is a MATLAB implementation of an IEKF for solving trajectory reconstruction problems, with modernization and algorithmic improvements over the original STEP code. Mathematical details of the filter formulation including process and measurement models can be found in [28].

B. Atmosphere Reconstruction

The InSight entry vehicle did not have the benefit of a heatshield instrumentation system to make direct measurements of the atmospheric environments during entry such as that used for MSL [29, 31]. Thus, the as-flown EDL atmosphere profile was reconstructed using the classical approach [32, 33] in which the nominal aerodynamic database [20] is used in conjunction with the measured accelerations and reconstructed wind-relative velocity (assuming the mean atmospheric winds) to compute an estimate of the freestream density simultaneously with the angles of attack and sideslip. Density is used with the reconstructed altitude and the gravity model to integrate the hydrostatic equation in

order to produce an estimate of the atmospheric pressure. Temperature is computed from the ideal gas law using a specific gas constant of $\Re$ = 190.7817 J/kg-K corresponding to an atmospheric composition of 96% CO2, 1.93% Ar and 1.89% N2 [34]. Uncertainties of the reconstruction are computed by means of linear covariance analysis [32, 33]. The reconstruction can be performed from the upper altitudes where there is sufficient signal in the axial acceleration up until just prior to parachute deployment. In theory the method can be used to reconstruct atmosphere while under the parachute, but the parachute drag coefficient is not well known and so the reconstruction is ceased prior to parachute deployment.

Since the atmosphere reconstruction does not cover the full altitude range from entry interface to the surface, other data must be utilized to estimate the full range of the as-flown atmosphere profile. For this work, a single case from the 100,000 dispersed 4.24 MCS ensemble was extracted that was a best fit to the reconstructed density. This profile provides a self-consistent atmosphere model from entry interface to the surface that represents the as-flown atmosphere profile. The match was determined from a weighted least-squares fit to the reconstructed density. The weighting was determined by the ratio of acceleration to the peak acceleration, so that the reconstructed density at the maximum deceleration where there is the best signal-to-noise ratio received the highest weight.

V. Reconstruction Results

A. Inertial Trajectory

Components of the vehicle trajectory relative to the Mars surface are shown in Figure 9 along with the OD133 initial conditions and the landing site location. Events along the trajectory are also indicated. Position and velocity uncertainties are shown in Figure 10. The planet-relative velocity magnitude and flight path angle are shown in Figure 11. The velocity magnitude at t_0 is 5542.2 m/s. The reconstructed initial relative flight path angle at t_0 is -12.57 deg. The peak deceleration during entry is 8.25 g. The reconstructed velocity magnitude at touchdown is 2.7 m/s. The vehicle body Euler angles relative to the North-East-Down frame along with the total attitude uncertainty are shown in Figure 12. The total attitude uncertainty is shown in 12(d). The entry capsule developed a roll rate during the dynamic pressure pulse that caused the vehicle to roll from its entry attitude of 180 deg to approximately 30 deg at the time of parachute deployment. The Mars Phoenix entry capsule exhibited similar behavior although of a lesser magnitude [35]. This roll behavior was not observed in pre-flight trajectory simulations and the root cause remains unknown [3].

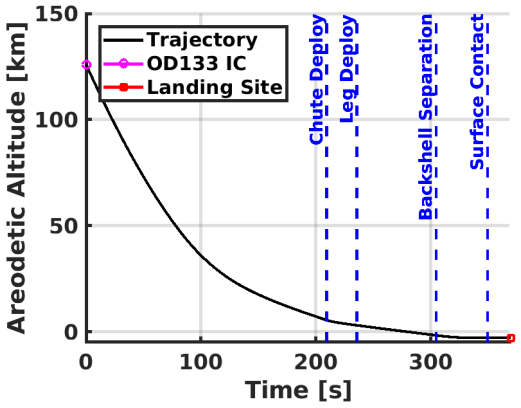

(a) Areodetic Altitude

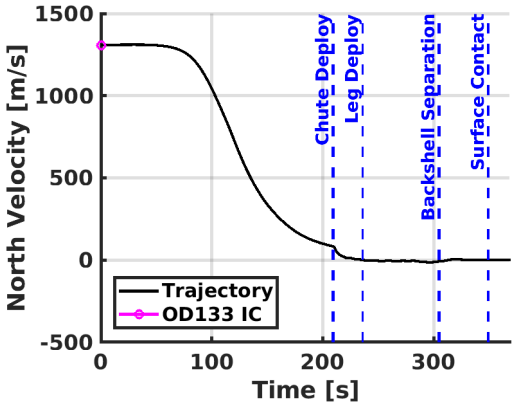

(b) North Velocity

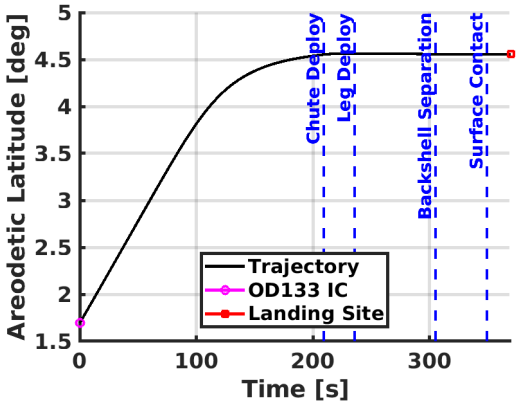

(c) Areodetic Latitude

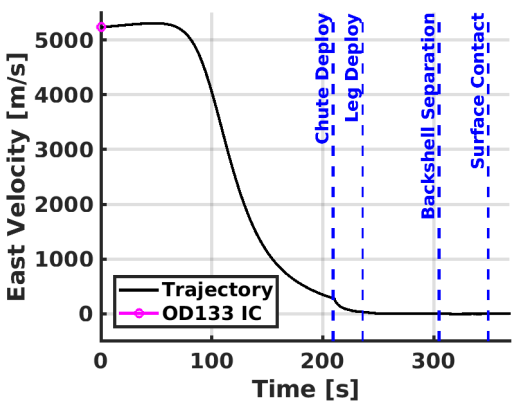

(d) East Velocity

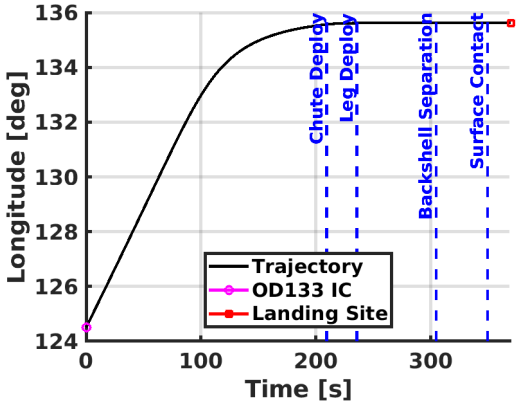

(e) Longitude

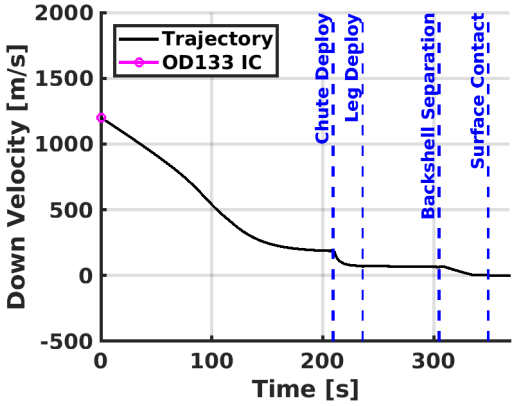

(f) Down Velocity

Fig. 9 Reconstructed Position and Velocity

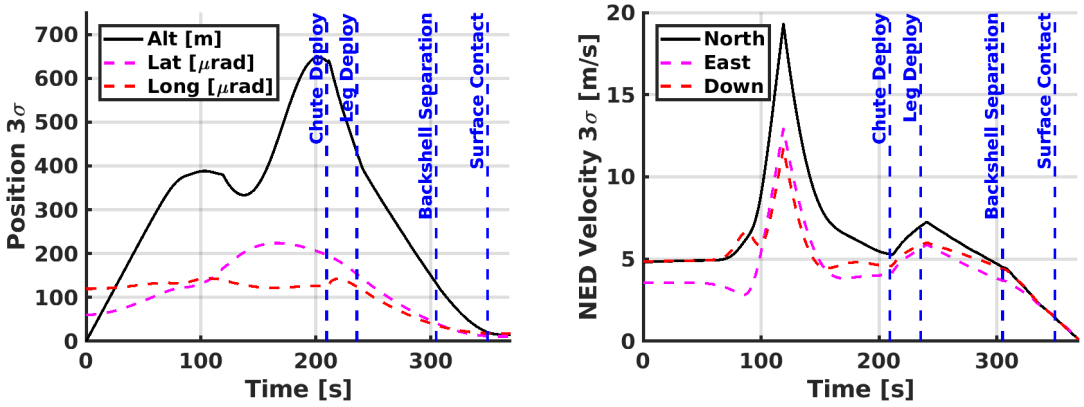

(a) Position (b) Velocity

Fig. 10 Reconstructed Position and Velocity Uncertainties

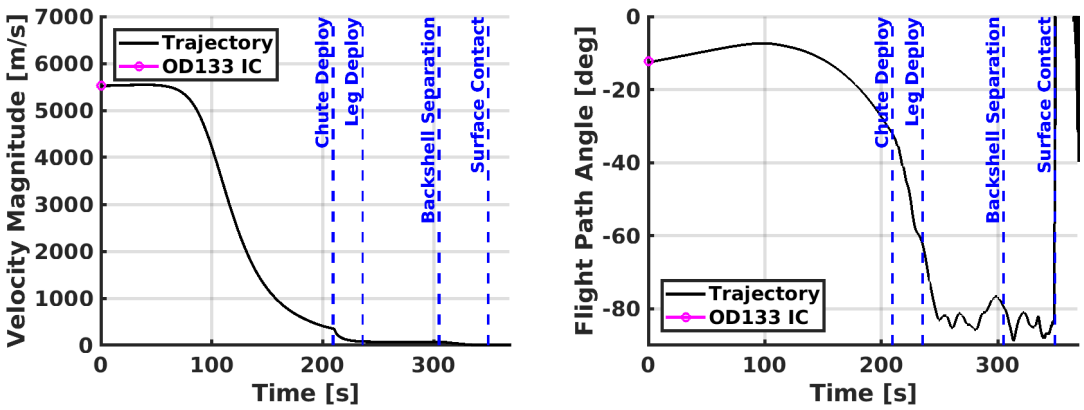

(a) Velocity Magnitude (b) Flight Path Angle

Fig. 11 Reconstructed Velocity and Flight Path Angle

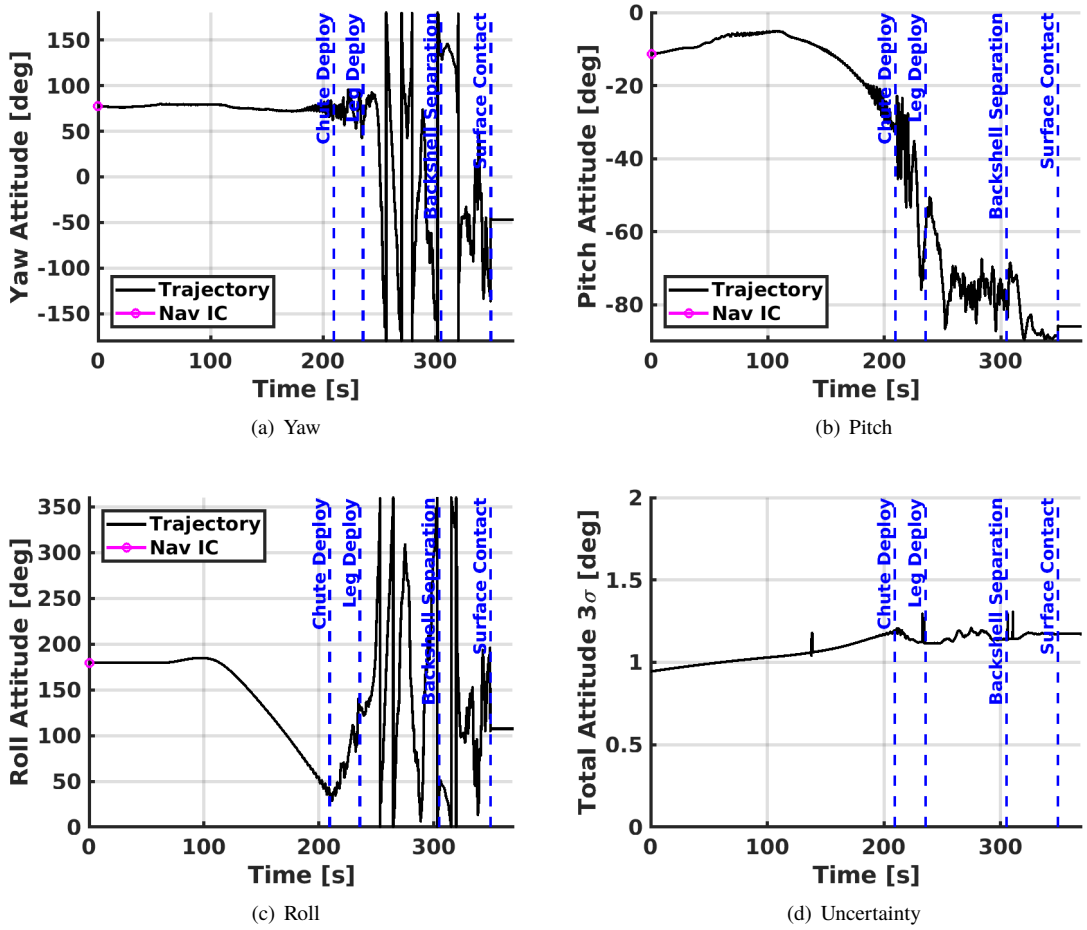

(a) Yaw

(b) Pitch

(c) Roll

(d) Uncertainty

Fig. 12 Reconstructed Attitude

B. Atmospheric-Relative Trajectory

This section describes the atmospheric-relative trajectory that was reconstructed from the inertial trajectory, accelerations, and the nominal aerodynamic database. Figure 13 shows the aerodynamic flow angles. Two sets of angles are shown. The first set is based on the inertial reconstructed trajectory with the nominal wind profile superimposed, labeled as IMU. The second set, labeled ADB, is based on the ratios of normal and side accelerations to the axial acceleration for determination of angle of attack and sideslip, respectively. In both cases there is clear signal that shows the hypersonic bounded instability. The ADB reconstructed angles are fairly noisy initially due to poor signal to noise ratio early in the trajectory where the dynamic pressure is low. The impact of the low signal to noise ratio is also evident in the ADB total angle of attack uncertainty shown in Figure 13(d).

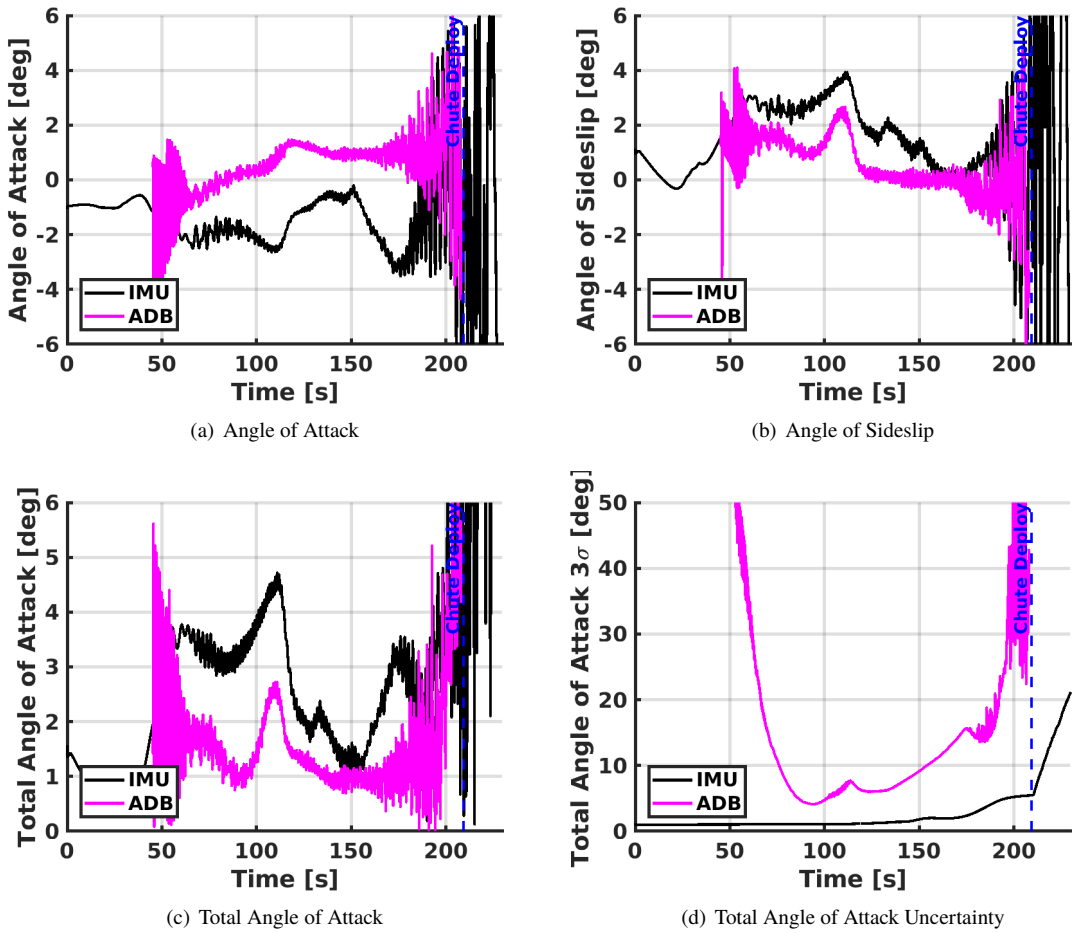

(a) Angle of Attack

(b) Angle of Sideslip

(c) Total Angle of Attack

(d) Total Angle of Attack Uncertainty

Fig. 13 Reconstructed Aerodynamic Angles

The reconstructed vehicle attitude and aerodynamic flow angles can be used to determine the direction of the aerodynamic accelerations relative to the planet. The flow angles provide the direction of the aerodynamic acceleration in body axes, based on the measured accelerations from the IMU. The body axis accelerations can then be transformed into a planet-relative frame using the reconstructed attitude angles. The results are shown in Figure 14 in which the direction of the lift and drag accelerations are shown as components in the NED frame. The reconstruction indicates that the lift direction was oriented downward toward the planet surface at entry. As the vehicle rolled during the dynamic pressure pulse, a component of the lift became directed toward the north. The orientation of the aerodynamic lift is considered to be one factor that explains the shortened EDL timeline and the uprange/crossrange location of the landing site relative to the target coordinates. Additional details of the entry capsule aerodynamic performance can be found in [36].

The reconstructed dynamic pressure and Mach number are shown in Figure 15. The vehicle reached a peak dynamic

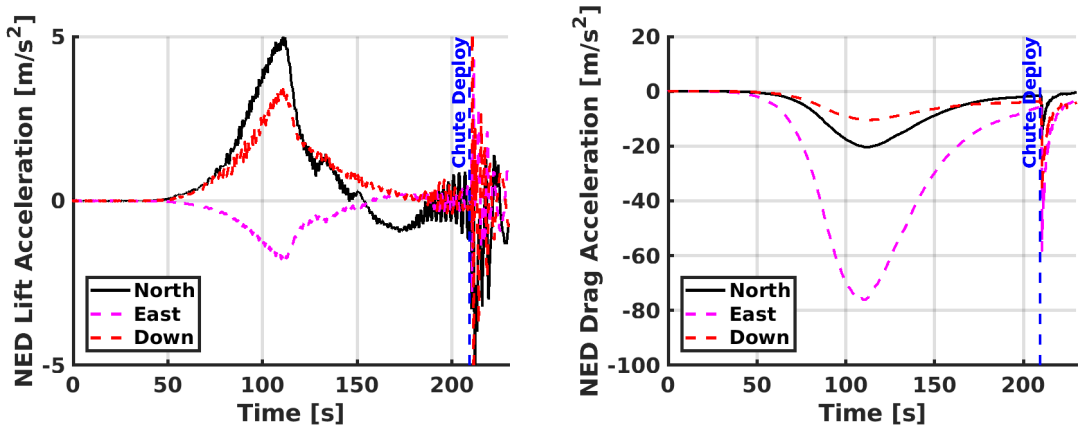

(a) Lift Acceleration (b) Drag Acceleration

Fig. 14 Lift and Drag Acceleration Components

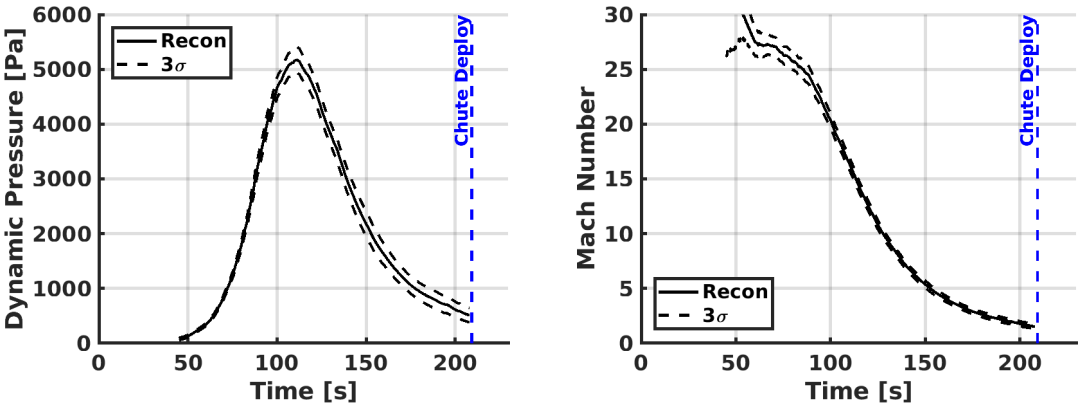

(a) Dynamic Pressure (b) Mach Number

Fig. 15 Reconsstructed Atmospheric-Relative Trajectory

pressure during entry of 5174 Pa at a Mach number of 15.87 and altitude of 30.33 km. The reconstructed conditions at parachute deployment indicate a dynamic pressure of 511.3 Pa and a Mach number of 1.522, occuring at an areodetic altitude of 5.523 km. The 3σ uncertainties of these reconstructed quantities are 128.1 Pa in dynamic pressure and 0.212 in Mach number, respectively.

C. Atmosphere

The reconstructed atmosphere is shown in Figure 16. This figure shows the reconstructed atmosphere and the 3σ uncertainties based on the nominal aerodynamics and measured acceleration, compared to the mean 4.24 MCS profile and its 3σ uncertainty bounds and the best fit atmosphere profile case from the 100,000 case ensemble. The atmosphere was reconstructed over the areodetic altitude range from 77.62 km to 5.64 km. The reconstructed density is roughly 1σ below the mean 4.24 MCS profile over the altitude range in which the reconstruction was performed. The reconstructed pressure is correspondingly below the 4.24 MCS mean profile. The consistent low density in the upper altitude regime is considered to be an important factor in the high deceleration and shortened timeline of the EDL operations. Due to the low density, the vehicle went deeper into the atmosphere before beginning to decelerate, thus encountering a higher density for any given velocity.

The best-fit model case matches the reconstructed density to roughly within 5% over the altitude range. The reconstructed density shows a low altitude feature in which the gradient reverses just prior to parachute deployment,

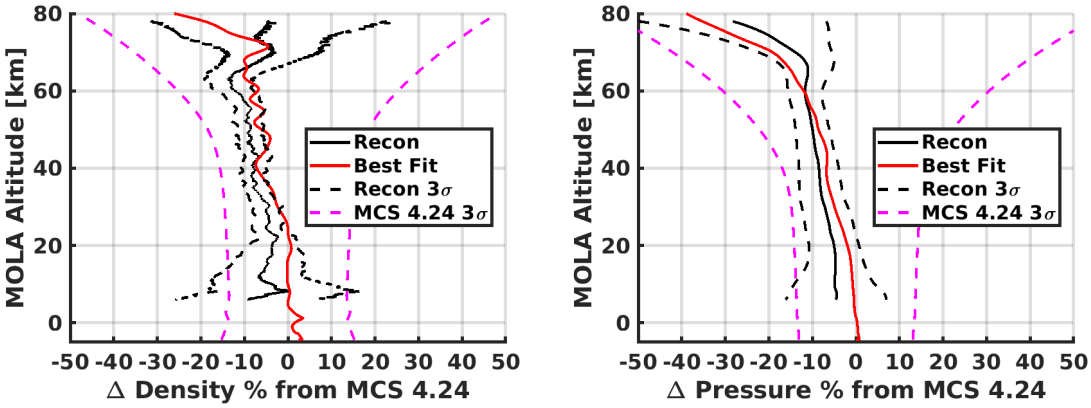

(a) Density Ratio

(b) Pressure Ratio

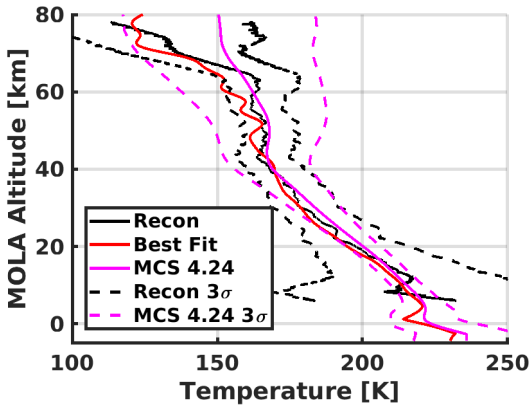

(c) Temperature

Fig. 16 Reconstructed Atmosphere

which also appears in the reconstructed temperature. This feature could either be caused by a wind shear (recall that the mean winds were assumed in the reconstruction) or the near surface boundary layer. Similar inversions were noted in the Mars Pathfinder and Mars Opportunity reconstructed atmospheres [37, 38], as well as the recent ExoMars Schiaparelli mission [39]. Interestingly the best-fit model case displays a similar feature due to the boundary layer, although it occurs at a lower altitude.

The best-fit model case is shown again in Figure 17 over the entire altitude range from entry interface to the surface. Since this profile is just one case from a Monte Carlo ensemble there is no associated uncertainty model. To be conservative, the 3σ bounds of the entire 100,000 case ensemble were applied to this profile. This profile matches the reconstructed density to within roughly 5% between 77 km to 10 km, over which the matching was performed. The surface pressure from this profile is 729.352 Pa which is also in agreement with the surface pressure at landing extrapolated from the pressure measurements made by the lander at the appropriate local mean solar time, which indicated a pressure of 733.724 Pa (6.865 Pa 3σ).

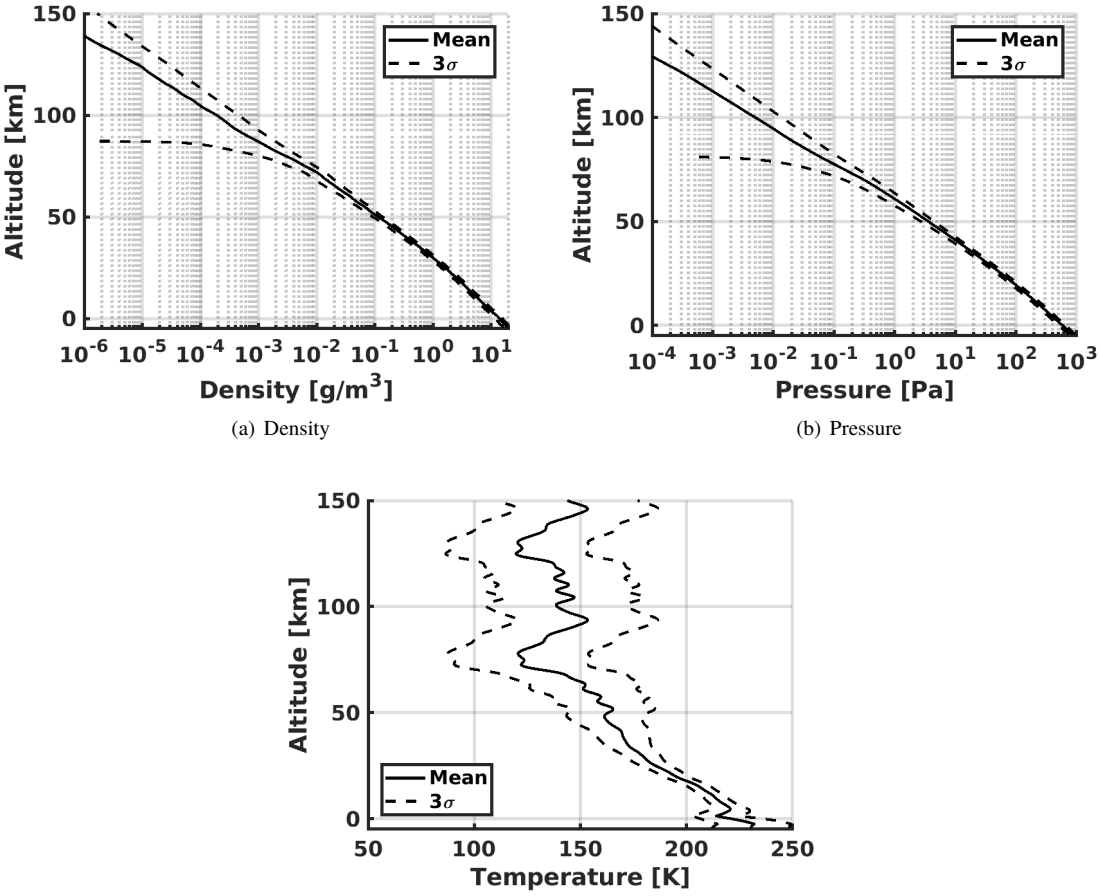

(a) Density

(b) Pressure

(c) Temperature

Fig. 17 Best-Fit Atmosphere

VI. Conclusions

The Mars InSight entry, descent, and landing trajectory was reconstructed using a Kalman filter to process inertial measurement unit data, radar altimeter data, orbit determination initial conditions, and landing site location. The atmosphere was then reconstructed using the on-board measured accelerations and the nominal aerodynamic database. The reconstructed atmosphere was roughly 1σ below the mean profile determined from Mars Climate Sounder measurements. The reconstructed vehicle attitude indicated that the aerodynamic lift vector was oriented downward toward the planet at entry and as the vehicle developed a roll rate, similar to Mars Phoenix, a component of the lift became directed toward the north. The combination of low density and the direction of the aerodynamic lift are deemed to be the factors that most likely causes the high deceleration, compressed EDL timeline, and the uptrack/crosstrack landing site location relative to the target coordinates. The reconstructed density was then matched to a case from an ensemble of 100,000 dispersed cases around the mean Mars Climate Sounder profile. The matched case agreed with the reconstruction to within 5% over the altitude range of the reconstruction. This profile provides a self-consistent atmosphere model from entry interface to the surface that represents the as-flown atmosphere profile during the Mars InSight entry, descent, and landing.

Acknowledgments

The reconstructed mass properties were provided by Mark Johnson. The 3σ wind uncertainty profiles shown in Figure 7 were computed by Jake Tynis. The OD133 initial covariance was provided by Robert Maddock. Radar uncertainties were provided by David Skulsky. Landing site location uncertainties were provided by Brooke Harper.

The authors are grateful to Alessio Aboudan and Francesca Ferri for pointing out the temperature inversions from the Pathfinder, Opportunity, and Schiaparelli reconstructions.

References

[1] Hoffman, T., "InSight: Mission to Mars," IEEE Aerospace Conference, March 2018.

[2] Grover, R. M., Cichy, B. D., and Desai, P., "Overview of the Phoenix Entry, Descent, and Landing System Architecture," *Journal of Spacecraft and Rockets*, Vol. 48, No. 5, 2011, pp. 706–712.

[3] Maddock, R. W., Dwyer-Cianciolo, A., Karlgaard, C. D., Korzun, A., Litton, D., and Zumwalt, C., "InSight Entry, Descent, and Landing Post-Flight Performance Assessment," AIAA Atmospheric Flight Mechanics Conference, Orlando, FL, January 2020 (submitted).

[4] Karlgaard, C. D., and Tynis, J. A., "Mars Phoenix EDL Trajectory Reconstruction Using NewSTEP," NASA TM 2019-220282, May 2019.

[5] Crassidis, J. L., and Junkins, J. L., *Optimal Estimation of Dynamic Systems*, CRC Press, Boca Raton, FL, 2004, Chapter 5.

[6] Tapley, B. D., Schutz, , B. E., and Born, G. H., *Statistical Orbit Determination*, Elsevier, 2004, Chapter 2.

[7] Winder, S., *Analog and Digital Filter Design, Second Edition*, Elsevier Science, 2002, Chapter 2.

[8] Cianciolo, A. D., Striepe, S., Carson, J., Sostaric, R., Woffinden, D., Karlgaard, C., Lugo, R., Powell, R., and Tynis, J., "Defining Navigation Requirements for Future Precision Lander Missions," AIAA Paper 2019–0661, January 2019.

[9] Blanchard, R. C. and Desai, P. N., "Mars Phoenix Entry, Descent, and Landing Trajectory and Atmosphere Reconstruction," *Journal of Spacecraft and Rockets*, Vol. 48, No. 5, 2011, pp. 809–821.

[10] Belz, J. E., Chen, C., and Cichy, B., "Phoenix Landing Radar Heatshield Anomaly," *Journal of Spacecraft and Rockets*, Vol. 48, No. 5, 2011, pp. 772—777.

[11] Abilleira, F., Halsell, A., Chung, M-K., Fuji, K., Gustafson, E., Hahn, Y., Lee, J., McCandless, S. E., Mottinger, N., Seubert, J., Sklyanskiy, E., and Wallace, M., "2018 Mars InSight Mission Design and Navigation Overview," American Astronautical Society, AAS Paper 18-251, January 2018.

[12] Abilleira, F., Halsell, A., Kruizinga, G., Bonfiglio, E., Grover, R., Chung, M-K., Fuji, K., Gustafson, E., Hahn, Y., Jefferson, D., Lau, E., Lee, J., McCandless, S. E., Mottinger, N., Seubert, J., Sklyanskiy, E., and Wallace, M., "2018 Mars InSight Trajectory Reconstruction and Performance from Launch through Landing," American Astronautical Society, AAS Paper 19-204, January 2019.

[13] Smith, D. E., Zuber, M. T., Frey, H. V., Garvin, J. B., Head, J. W., Muhleman, D. O., Pettengill, G. H., Phillips, R. J., Solomon, S. C., Zwally, H. J., Banerdt, W. B., Duxbury, T. C., Golombek, M. P., Lemoine, F. G., Neumann, G. A., Rowlands, D. D., Aharonson, O., Ford, P. G., Ivanov, A. B., Johnson, C. L., McGovern, P. J., Abshire, J. B., Afzal, R. S., and Sun, X., "Mars Orbiter Laser Altimeter: Experiment Summary After the First Year of Global Mapping of Mars," *Journal of Geophysical Research*, Vol. 106, No. E10, pp. 23,689–23,722, 2001.

[14] McEwan, A., Eliason, E. M., Bergstrom, J. W., Bridges, N. T., Hansen, C. J., Delamere, W. A., Grant, J. A., Gulick, V. C., Herkenhoff, K. E., Keszthelyi, L., Kirk, R. L., Mellon, M. T., Squyres, S. W., Thomas, N., Weitz, C. M., "Mars Reconnaissance Orbiter's High Resolution Imaging Science Experiment (HiRISE)," *Journal of Geophysical Research*, Vol. 112, No. E5, 2007, Paper E05S02.

[15] McCleese, D. J., Schofield, J. T., Taylor, F. W., Calcutt, S. B., Foote, M. C., Kass, D. M., Leovy, C. B., Paige, D. A., Read, P. L., and Zurek, R. W., "Mars Climate Sounder: An Investigation of Thermal and Water Vapor Structure, Dust and Condensate Distributions in the Atmosphere, and Energy Balance of the Polar Regions," *Journal of Geophysical Research*, Vol. 112, No. E5, 2007, Paper E05S06.

[16] Golombek, M., Kipp, D., Warner, N., Dauber, I., Fergason, R., Kirk, R., Beyer, R., Huertas, A., Piqueux, S., Putzig, N., Campbell, B., Morgan, G., Charalambous, C., Pike, W., Gwinner, K., Calef, F., Kass, D., Mischna, M., Ashley, J., Bloom, C., Wigton, N., Hare, T., Schwartz, C., Gengl, H., Redmond, L., Trautman, M., Sweeney, J., Grima, C., Smith, I., Sklyanskiy, E., Lisano, M., Bernadini, J., Smrekar, S., Lognonne, P., and Banerdt, W., "Selection of the InSight Landing Site," *Space Science Reviews*, Vol. 211, Nos. 1–4, 2017, pp. 5–95.

[17] Banfield, D., Rodriguez-Manfredi, J. A., Russell, C. T., Rowe, K. M., Leneman, D., Lai, H. R., Cruce, P. R., Means, J. D., Johnson, C. L., Mittelholz, A., Joy, S. P., Chi, P. J., Mikellides, I. G., Carpenter, S., Navarro, S., Sebastian, E., Gomez-Elvira, J., Torres, J., Mora, L., Peinado, V., Lepinette, A., Hurst, K., Lognonne, P., Smrekar, S. E., and Banerdt, W. B., "InSight Auxiliary Payload Sensor Suite (APSS)," *Space Science Reviews*, Vol. 215, No. 4, 2019.

[18] Spiga, A., Banfield, D., Teanby, N. A., Forget, F., Lucas, A., Kenda, B., Rodriguez-Manfredi, J. A., Widmer-Schnidrig, R., Murdoch, N., Lemmon, M. T., Garcia, R. F., Martire, L., Karatekin, O., Le Maistre, S., Van Howe, B., Dehant, V., Lognonne, P., Mueller, N., Lorenz, R., Mimoun, D., Rodriguez, S., Beucler, E., Dauber, I., Golombek, M. P., Bertrand, T., Nishikawa, Y., Millour, E., Rolland, L., Brissaud, Q., Kawamura, T., Mocquet, A., Martin, R., Clinton, J., Stutzmann, E., Spohn, T., Smrekar, S., and Banerdt, W. B., "Atmospheric Science with InSight," *Space Science Reviews*, Vol. 214, No. 109, 2018.

[19] Gomez-Elvira, J., Armiens, C., Castaner, L., Dominguez, M., Genzer, M., Gomez, F., Haberle, R., Harri, A.-M., Jimenez, V., Kahanpaa, H., Kowalski, L., Lepinette, A., Martin, J., Martinez-Frias, J., McEwan, I., Mora, L., Moreno, J., Navarro, S., de Pablo, M. A., Peninado, V., Pena, A., Polkko, J., Ramos, M., Renno, N. O., Ricart, J., Richardson, M., Rodriguez-Manfredi, J., Romeral, J., Sebastian, E., Serrano, J., de la Torre Juarez, M., Torres, J., Torrero, F., Urqui, R., Vazquez, L., Velasco, T., Verdasca, J., Zorzano, M.-P., and Martin-Torres, J., "REMS: The Environmental Sensor Suite for the Mars Science Laboratory Rover," *Space Science Reviews*, Vol. 170, No. 1–4, 2012, pp. 583–640.

[20] Edquist, K. T., Desai, P. N., and Schoenenberger, M., "Aerodynamics for Mars Phoenix Entry Capsule," *Journal of Spacecraft and Rockets*, Vol. 48, No. 5, 2011, pp. 713–726.

[21] Schoenenberger, M., Cheatwood, F. M., and Desai, P. N., "Static Aerodynamics of the Mars Exploration Rover Entry Capsule," AIAA paper 2005-56, January 2005.

[22] Spencer, D. A., Blanchard, R. C., Braun, R. D., Kallemeyn, P. H., and Thurman, S. W., "Mars Pathfinder Entry, Descent, and Landing Reconstruction," *Journal of Spacecraft and Rockets*, Vol. 36, No. 3, 1999, pp. 357–366.

[23] Konopliv, A. S., Asmar, S. W., Folkner, W. M., Karatekin, O., Nunes, D. C., Smrekar, S. E., Yoder, C. F., and Zuber, M. T., "Mars High Resolution Gravity Fields from MRO, Mars Seasonal Gravity, and Other Dynamical Parameters," *Icarus*, Vol. 211, No. 1, 2011, pp. 401–428.

[24] Wagner, W. E., "Re-Entry Filtering, Prediction, and Smoothing," *Journal of Spacecraft and Rockets*, Vol. 3, No. 9, 1966, pp. 1321–1327.

[25] Wagner, W. E. and Serold, A. C., "Formulation on Statistical Trajectory Estimation Programs," NASA CR-1482, January 1970.

[26] Karlgaard, C. D., Tartabini, P. V., Blanchard, R. C., Kirsch, M., and Toniolo, M. D., "Hyper–X Post–Flight Trajectory Reconstruction," *Journal of Spacecraft and Rockets*, Vol. 43, No. 1, 2006, pp. 105–115.

[27] Karlgaard, C. D., Tartabini, P. V., Martin, J. G., Blanchard, R. C., Kirsch, M., Toniolo, M. D., and Thornblom, M. N., "Statistical Estimation Methods for Trajectory Reconstruction: Application to Hyper-X," NASA TM-2009-215792, August 2009.

[28] Karlgaard, C. D., Beck, R. E., Derry, S. D., Brandon, J. M., Starr, B. R., Tartabini, P. V., and Olds, A. D., "Ares I-X Trajectory Reconstruction: Methodology and Results," *Journal of Spacecraft and Rockets*, Vol. 50, No. 3, 2013, pp. 641–661.

[29] Karlgaard, C. D., Kutty, P., Schoenenberger, M., Munk, M. M., Little, A. D., Kuhl, C. A., and Shidner, J., "Mars Science Laboratory Entry Atmospheric Data System Trajectory and Atmosphere Reconstruction," *Journal of Spacecraft and Rockets*, Vol. 51, No. 4, 2014, pp. 1029–1047.

[30] Karlgaard, C. D., Kutty, P., O'Farrell, C., Blood, E. M, Ginn, J., and Schoenenberger, M., "Reconstruction of Atmosphere, Trajectory, and Aerodynamics for the Low Density Supersonic Decelerator Test Vehicles," *Journal of Spacecraft and Rockets*, Vol. 56, No. 1, 2019, pp. 221–240.

[31] Chen, A., Cianciolo, A., Vasavada, A., Karlgaard, C., Barnes, J., Cantor, B., Hinson, D., Kass, D., Lewis, S., Mischna, M., Rafkin, S., Tyler, D., "Reconstruction of Atmospheric Properties from the Mars Science Laboratory Entry, Descent, and Landing," *Journal of Spacecraft and Rockets*, Vol. 51, No. 4, 2014, pp. 1062–1075.

[32] Kutty, P. and Karlgaard, C. D., "Mars Science Laboratory Aerodatabase Trajectory Reconstruction and Uncertainty Assessment," AIAA Paper 2014-1094, January 2014.

[33] Kutty, P., "Reconstruction and Uncertainty Quantification of Entry, Descent, and Landing Trajectories Using Vehicle Aerodynamics," M. S. Thesis, School of Aerospace Engineering, Georgia Institute of Technology, May 2014.

[34] Mahaffy, P. R., Webster, C. R., Atreya, S. K., Franz, H., Wong, M., Conrad, P. G., Harpold, D., Jones, J. J., Leshin, L. A., Manning, H., Owen, T., Pepin, R. O., Squyres, S., and Trainer, M., "Abundance and Isotopic Composition of Gases in the Martian Atmosphere from the Curiosity Rover," *Science*, Vol. 341, July 2013, pp. 263—265.

[35] Desai, P. N., Prince, J. L., Queen, E. M., Schoenenberger, M., Cruz, J. R., and Grover, M. R., "Entry, Descent, and Landing Performance of the Mars Phoenix Lander," *Journal of Spacecraft and Rockets*, Vol. 48, No. 5, 2011, pp. 798–808.

[36] Korzun, A., Maddock, R. W., Schoenenberger, M., Edquist, K. T., Zumwalt, C., and Karlgaard, C. D., "Aerodynamic Performance of the 2018 Mars InSight Lander," AIAA Atmospheric Flight Mechanics Conference, Orlando, FL, January 2020 (submitted).

[37] Magalhaes, J. A., Schofield, J. T., and Sieff, A., "Results of the Mars Pathfinder Atmospheric Structure Investigation," *Journal of Geophysical Research*, Vol. 104, No. E4, 1999, pp. 8943–8955.

[38] Withers, P. and Smith, M. D., "Atmospheric Entry Profiles from the Mars Exploration Rovers Spirit and Opportunity," *Icarus*, Vol. 185, No. 1, 2006, pp. 133–142.

[39] Aboudan, A., Colombatti, G., Bettanini, C., Ferri, F., Lewis, S., Van Hove, B., Karatekin, O., and Debei, S., "ExoMars 2016 Schiaparelli Module Trajectory and Atmospheric Profiles Reconstruction: Analysis of the On-board Inertial and Radar Measurements," *Space Science Reviews*, Vol. 214, No. 97, 2018, pp. 1–31.